Astronomy & Astrophysics manuscript no. output
June 30, 2026

Searching for the elusive CH_2^+ with the James Webb Space Telescope

Another carbocation to constrain astrochemical networks

M. Zannese[1,2], L. H. Coudert[3], E. Dartois[3], P. Dell'Ova[2], O. Roncero[1] P. del Mazo-Sevillano[4], U. Jacovella[3], B. Gans[3], J. R. Goicoechea[1], D. Van De Putte[5,6,7], C. Boersma[8], E. Habart[2], E. Peeters[5,6,10], J. Cami[5,6], and R. Chown[9], I. Schroetter[11], O. Kannavou[2]

[1] Instituto de Física Fundamental (CSIC). Calle Serrano 121-123, 28006, Madrid, Spain
e-mail: m.zannese@iff.csic.es
[2] Institut d'Astrophysique Spatiale, Université Paris-Saclay, CNRS, Bâtiment 121, 91405 Orsay Cedex, France
[3] Institut des Sciences Moléculaires d'Orsay, UMR8214, CNRS, Université Paris-Saclay, 91405 Orsay, France
[4] Departamento de Química Física, Facultad de Ciencias Químicas, Universidad de Salamanca , 37008 Salamanca, Spain
[5] Department of Physics & Astronomy, The University of Western Ontario, London ON N6A 3K7, Canada
[6] Institute for Earth and Space Exploration, The University of Western Ontario, London ON N6A 3K7, Canada
[7] Space Telescope Science Institute, 3700 San Martin Drive, Baltimore, MD, 21218, USA
[8] NASA Ames Research Center, MS 245-6, Moffett Field, CA 94035-1000, USA
[9] Department of Astronomy, The Ohio State University, 140 West 18th Avenue, Columbus, OH 43210, USA
[10] Carl Sagan Center, SETI Institute, 339 Bernardo Avenue, Suite 200, Mountain View, CA 94043, USA
[11] Institut de Planétologie et d'Astrophysique de Grenoble (IPAG), Université Grenoble Alpes, CNRS, F-38000 Grenoble, France

Received April 15, 2026; accepted

ABSTRACT

Context. Carbocations are key species in interstellar chemistry, providing entry points for building larger hydrocarbons. CH^+ , and more recently, CH_3^+, have been detected. Other carbocations await detection to provide a comprehensive view of the astrochemical network that is at work in the interstellar medium.
Aims. We search for CH_2^+ in objects in which CH_3^+ was detected and evaluate the most favorable conditions for detecting the elusive CH_2^+ reactive cation.
Methods. We calculated the CH_2^+ rotational and rovibrational transitions expected to contribute in the mid- to far-infrared, focusing on the lower-energy rovibrational levels. We then calculated CH_2^+ infrared emission spectra at different excitation temperatures and compared them to JWST spectra of the externally irradiated disk d203-506 in Orion, where CH^+ and CH_3^+ have already been detected. We used thermochemical models to predict the abundance and spatial morphology of CH_2^+ to better understand its nondetection.
Results. The comparison to JWST spectra allowed us to provide excitation-temperature-dependent upper limits to the excited column density. These are several times lower than those detected for CH^+ and CH_3^+ in their excited states. Based on model calculations for photodissociation regions and assuming similar excitation temperatures, the upper limit derived from observations and CH_2^+ model spectrum is either slightly above or below the column density expected from models of photodissociation regions. We provide a list of tabulated transitions to allow the community to search for this carbocation in future observations as CH_2^+ is key in providing observational constraints on astrochemical models.

1. Introduction

In dense interstellar clouds, the majority of small molecules are expected to be produced by gas-phase ion-neutral reactions (see Fig. 1). The carbon ion chemistry is initiated by C^+, which is particularly abundant in ultraviolet (UV)-irradiated regions, or H_3^+, which is enhanced by cosmic rays as well as UV radiation (Goicoechea et al. 2025b). It is then followed by reactions with H_2 or C (Smith 1992; Indriolo et al. 2010; Herbst 2021),

$$C^+ \xrightarrow{H_2} CH^+ \xrightarrow{H_2} {CH_2}^+ \xrightarrow{H_2} {CH_3}^+ \quad (1)$$

$$H_3{}^+ \xrightarrow{C} CH^+ \xrightarrow{H_2} {CH_2}^+ \xrightarrow{H_2} {CH_3}^+. \quad (2)$$

CH_3^+ then undergoes dissociative recombination, producing C, CH, or CH_2, which can then react with C^+ to produce larger molecules. In this context, CH_2^+ is an essential intermediate step in the carbocation chain leading to the formation of larger carbonaceous species. It thereby plays a pivotal role in astrochemical models as it is located in the molecular ladder between CH^+ and CH_3^+.

H_3^+ is now readily observed (Geballe & Oka 1996; Geballe 2006) and offers a way to determine the degree of ionization in diffuse clouds (e.g., McCall et al. 2002; Goto et al. 2008; Indriolo & McCall 2012). The same holds for CH^+, which was observed a long time ago, first in absorption in the diffuse interstellar medium (Douglas & Herzberg 1941) and then in emission in various environments (e.g., Cernicharo et al. 1997; Naylor et al. 2010; Wesson et al. 2010; Falgarone et al. 2010; Bruderer et al. 2010; Thi et al. 2011; Spinoglio et al. 2012; Rangwala et al. 2014; Morris et al. 2016). In contrast, CH_3^+ has only recently been detected outside the Solar System, with the *James Webb Space Telescope* (JWST) in the externally irradiated disk d203-506 near the Orion Bar (Berné et al. 2023;

Article published by EDP Sciences, to be cited as https://doi.org/10.1051/0004-6361/202660602

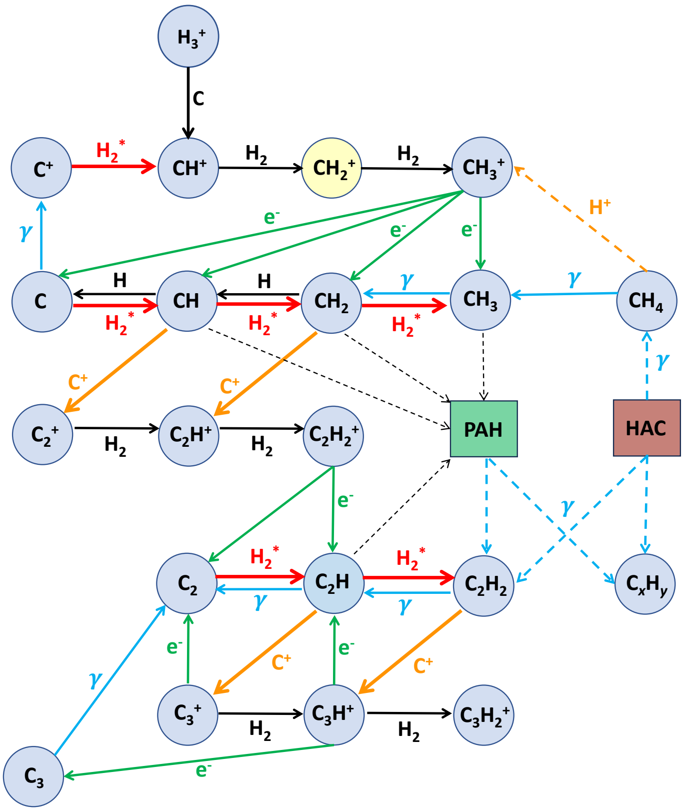

Fig. 1. Carbon ion chemistry network. The red arrows indicate endoergic reactions, which proceed rapidly at high T or in regions with significant FUV-pumped H_2^*. We also show possible reactions (dashed) involving Polyaromatic Hydrocarbon (PAH) and Hydrogenated Amorphous Carbon (HAC) grains, which may be relevant in certain conditions. The figure is adapted from Goicoechea et al. (2025a).

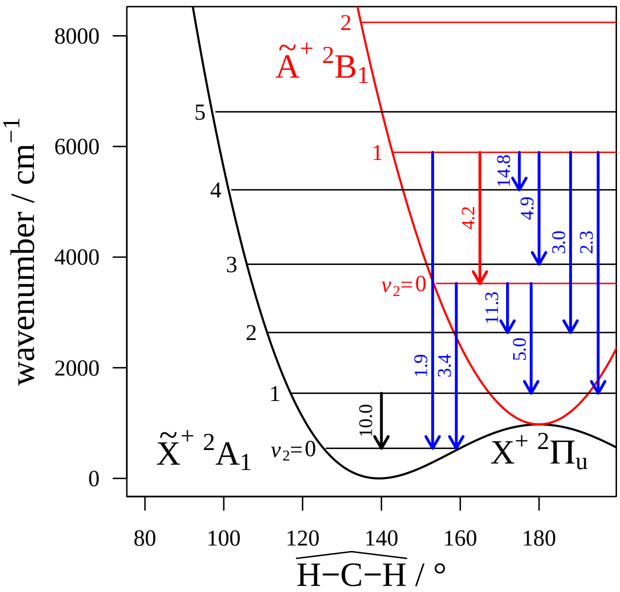

Fig. 2. Energy-level diagram of the bending levels, with no quanta in either stretching modes, in the two lowest electronic states of CH_2^+. These states result from the Renner-Teller coupling, which splits the doubly degenerate $^2\Pi_u$ state into two nondegenerate states for nonlinear configurations. The allowed vibrational (black for the fundamental $\tilde{X}^+\ ^2A_1$ state, red for the $\tilde{A}^+\ ^2B_1X$ state) and vibronic (blue) transitions are shown and labeled by their wavelength in μm. The bending potentials are plotted as a function of the bending angle ∠HCH in degrees. The potential curves and vibrational level positions are adapted from Jensen et al. (1995a) and Coudert et al. (2018).

Changala et al. 2023). This was joined with the detection of the rovibrational emission of CH^+ in the disk and the Bar itself, which provided insight into the carbocation chain chemistry by unveiling correlations between H_2, CH^+, and CH_3^+, which confirms the consecutive hydrogen abstractions (Zannese et al. 2025). It also led to additional detections of CH_3^+ in UV-irradiated environments (Henning et al. 2024; Bhatt et al. 2025; Volz et al. 2026). However, surprisingly, CH_2^+ remains undetected through its rovibrational emission expected in the mid-infrared (JWST) and its rotational emission expected in the far-infrared (*Infrared Space Observatory* and *Herschel*/PACS). Upper limits on the abundance of CH_2^+ can thus provide additional constraints on astrochemical models (e.g., confirming the validity of the nondetection with models).

We present a calculation of the CH_2^+ infrared (IR) spectrum in the range spanned by JWST. We built a line-list, consisting of line positions (in cm^{-1}) and line intensities in LTE conditions, which allowed us to evaluate the observational constraints arising from the nondetection of CH_2^+ in objects in which CH^+ and CH_3^+ are detected. In Sect. 2 we quantitatively describe the main features of the complex CH_2^+ spectroscopy. Sect. 3 is devoted to the modeling of the CH_2^+ spectrum and to the building of a spectroscopic database for astrophysical purposes. In Sect. 4 we constrain the nondetection of CH_2^+ emission in d203-506, a reference target in which CH_3^+ is well detected, and we derive an upper limit of its excited column density. In Sect. 5 we present a fiducial Photodissociation Regions (PDR) model of d203-506 to analyze the predicted abundance and morphology of CH_2^+. We then discuss the results and conclude with future prospects for CH_2^+ detection.

2. CH_2^+ spectroscopy

CH_2^+ possesses three vibrational modes: the symmetric stretching mode (ν_1), the bending mode (ν_2), and the asymmetric stretching mode (ν_3). Their corresponding fundamentals in its electronic ground state are located near 2883.0 cm^{-1} (∼3.47 μm; Kraemer et al. 1994), 995.5 cm^{-1} (∼10.05 μm; Kraemer et al. 1994), and 3131.4 cm^{-1} (∼3.19 μm; Rösslein et al. 1992), respectively. Although carbocations may behave very differently from the spectroscopic point of view, the observed transitions usually originate from the least energetic vibrational levels within their electronic ground state when they are detected in space based on their IR emission. Following the logic behind the detection of CH^+ and CH_3^+ (observed through their least energetic vibrational levels), the detection of CH_2^+ based on the emission from ν_2 would therefore be expected at around 10 μm. However, it is very difficult to model the gas-phase emission spectrum of this band accurately. There are no spectroscopic measurements of this band as the available spectroscopic information concerns the rotational constants of the ground state (Rösslein et al. 1992; Willitsch & Merkt 2003; Gottfried & Oka 2004) and the ν_3 band (Wang et al. 2013). In addition to this, the modeling of the ν_2 band is a theoretical challenge (Osmann et al. 1997; Bunker et al. 2001, 2007; Jensen et al. 1995a; Coudert et al. 2018; Solomonik & Yachmenev 2008) as the ν_2 mode is a large-amplitude motion and the active mode of a strong vibronic coupling known as the Renner-Teller effect (Herzberg 1966; Jungen 2019). Spectroscopic information about the ν_2 band can currently only be retrieved from the theoretical work of Osmann et al. (1997), who predicted that this band lies between 800 and 1100 cm^{-1}.

These results led to the search for CH_2^+ emission features between 9 and 11 μm. That CH_2^+ was not detected in any of the sources in which CH^+ and CH_3^+ were detected raises the question why these molecules can be identified by their near- and mid-IR emission fingerprints while the former cannot, even though astrochemical models suggest comparable abundances for CH_2^+ and CH^+ (see Sect. 5). One crucial difference between the CH^+ and CH_3^+ carbocations and CH_2^+ is the close-by electronic state for the latter. In its linear configuration, CH_2^+ indeed has a doubly degenerate $^2\Pi_u$ electronic ground state. The aforementioned Renner-Teller effect corresponds to the coupling between the electronic and bending vibrational degrees of freedom (ν_2 mode), which splits the $^2\Pi_u$ electronic state into distinct $\tilde{X}^+\,^2A_1$ and $\tilde{A}^+\,^2B_1$ nondegenerate states, as illustrated in Figure 2. That we do not know how the levels originating from the $\tilde{A}^+\,^2B_1$ state are populated, hence the importance of the transitions involving these levels in the CH_2^+ spectrum, makes it more difficult to validate the consistency with models of the nondetection of CH_2^+ based on the signal-to-noise ratio reached by JWST in the 10 μm range alone. The transitions expected in this range belong to the ν_2 band, and their frequency is altered by the Renner-Teller coupling. To constrain the detection of the transitions belonging to this band, we model these transitions in the next sections.

3. Calculations

The high-resolution spectrum of the CH_2^+ molecular ion is difficult to model and constrain for multiple reasons. (*i*) This ion is a highly reactive species that is difficult to produce and study spectroscopically. Consequently, it remains a significant challenge to experimentally constrain the accuracy of the models designed to reproduce its spectroscopic behavior. (*ii*) It is a floppy molecule characterized by a low barrier to linearity of about 1000 cm^{-1}. Even in its ground vibrational state, CH_2^+ can sample its linear configuration, leading to a theoretically infinite A rotational constant. The resulting strong vibration-rotation coupling leads to quasi-linearity (Carter & Handy 1982) and to rotational energies differing from those of an asymmetric top molecule. (*iii*) As already stated in Sect. 2, its $^2\Pi_u$ ground electronic state is split into a lower $\tilde{X}^+\,^2A_1$ and an upper $\tilde{A}^+\,^2B_1$ state by the Renner-Teller coupling.

In the approach we used to model the spectrum, the Schrödinger equation was solved simultaneously for all three vibrational modes and for the overall rotation. The Renner-Teller coupling was taken into account using the adiabatic representation. The calculation relied on the tridimensional potential energy surface of Kraemer et al. (1994) updated by Jensen et al. (1995a) to reproduce the ν_3 band measurements of Rösslein et al. (1992) better. The spin-orbit coupling was taken into account using the spin-orbit Hamiltonian given in Jensen et al. (1995a), which was retrieved from the results of Reuter & Peyerimhoff (1992). The line strengths were computed using the dipole moment surfaces reported by Osmann et al. (1997).

Our approach is an extension of two previous calculations. The first calculation, about the photoelectron spectrum of the methylene radical (Coudert et al. 2018), included all the effects described above, except those arising from the asymmetry leading to $|\Delta K| > 0$ matrix elements. The second calculation, dealing with the strong quasi-linearity of the non-rigid FH_2^+ ion (Gutlé & Coudert 2012), accounted exactly for the asymmetry, but there is no Renner-Teller coupling in this species.

The high-resolution spectrum of CH_2^+ has been the subject of several investigations by Bunker and coworkers (Kraemer et al. 1994; Osmann et al. 1997; Bunker et al. 2001). The investigation of Osmann et al. (1997) was carried out using the same potential, spin-orbit, and dipole moment surfaces as we used here, but a different theoretical treatment based on the MORBID approach (Jensen et al. 1995b). A comparison between the transition wavenumber calculated in this work and the wavenumbers from Osmann et al. (1997) reveals discrepancies of about 0.05 cm^{-1} for pure rotational transitions and of about 0.5 cm^{-1} for transitions belonging to the fundamental bands ν_1, ν_2, and ν_3. For the line strengths, we tend to have small discrepancies, of about 10%, for strong transitions and larger discrepancies, of about 50%, for weak transitions. It is unclear whether these discrepancies are due to the different nature of the theoretical approaches or to round-off errors arising when extracting spectroscopic parameters from tables of spectroscopic constants.

The first result of our calculation was a list of energy levels assigned in terms of rotational quantum numbers $N_{K_aK_c}$, vibrational quantum numbers ($v_1v_2v_3$), electronic states, and electron spin-rotation labels F_1 and F_2. Denoting J the quantum number for the total angular momentum $\mathbf{J} = \mathbf{N} + \mathbf{S}$, F_1 and F_2 correspond to $J = N + \frac{1}{2}$ and $N - \frac{1}{2}$, respectively. A maximum value of N equal to 10 and an energy cutoff of 13000 cm^{-1} were taken. The $N = 0$ level belonging to the ground vibrational state of the $\tilde{X}^+\,^2A_1$ electronic state was chosen as the zero reference energy. Table B.1 reports low-lying levels with $N \leq 3$ and an energy lower than 1200 cm^{-1}. The second result is a line list with assignments, calculated frequencies, line strengths, and Einstein coefficients. For a transition from upper (u) to lower (l) state, the Einstein coefficient A_{ul} in s^{-1} was calculated from the line strength using

$$A_{ul} = \frac{4(2\pi)^3 10^{-36}\, \nu_{ul}^3\, S_{ul}}{3\hbar g_u}, \tag{3}$$

where ν_{ul} is the wavenumber in cm^{-1}, S_{ul} is the strength in Debye[2], $\hbar$ is $6.626\,075\,5 \times 10^{-27}/2\pi$, and g_u is the statistical weight of the upper level, excluding statistical nuclear weights. In our case, $g_u = 2J_u + 1$. Table C.1 shows a portion of the lines list for transitions with $N \leq 5$ and $\nu \leq 60$ cm^{-1}. The entire lists of levels and transitions are available via Zenodo.[1]

4. Comparison to JWST observations

Of the sources in which CH_3^+ has been detected (Berné et al. 2023; Changala et al. 2023; Henning et al. 2024; Bhatt et al. 2025; Volz et al. 2026), the externally irradiated disk d203-506 observed in the field of view of the PDRs4All observations (Berné et al. 2023) has the highest detection in terms of signal-to-noise ratio and is favorable in terms of excitation conditions for CH_2^+ to emit in the mid-IR (see Sect. 6.1). Using the result of the calculations presented in the previous section, we compared the modeled emission spectra of CH_2^+ to the spectrum of d203-506, where CH^+ has also been detected.

We used the observations of the MIRI-MRS integral field unit (IFU) mode from the Early Release Science (ERS) program

[1] https://doi.org/10.5281/zenodo.18892632

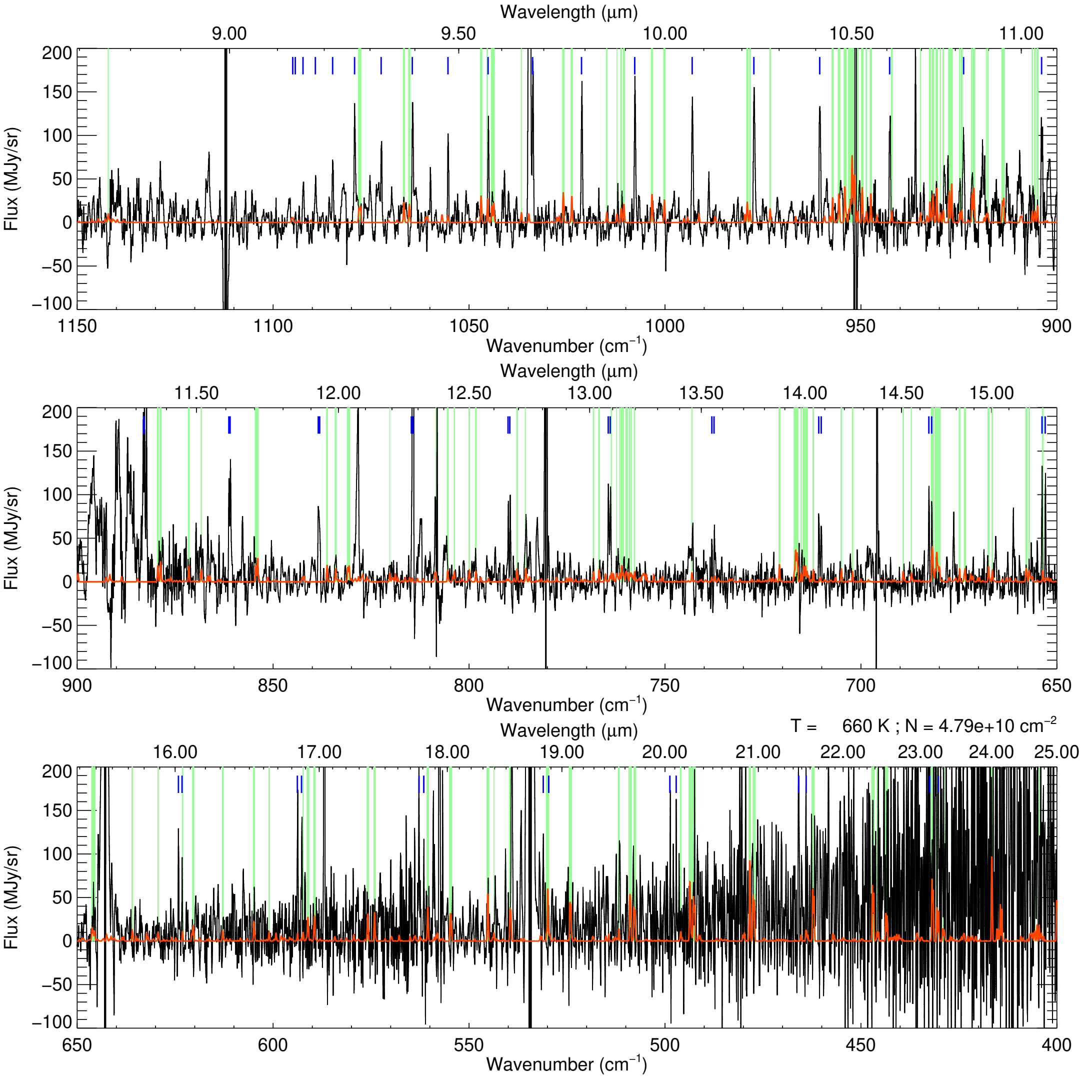

Fig. 3. Comparison of the irradiated disk d203-506 continuum-subtracted JWST spectrum to the CH_2^+ calculated LTE spectrum at 660 K with a column density limit corresponding to 4.8×10^{10} cm^{-2} (red). The series of emission lines labeled with vertical blue marks corresponds to the OH emission reported in Zannese et al. (2024). The vertical green shaded regions indicate the CH_2^+ lines used to constrain the upper limit derived at that excitation temperature.

PDRs4All[2]: Radiative feedback from massive stars (ID1288, PIs: Berné, Habart, Peeters, Berné et al. 2022). The data were reduced using the JWST science pipeline (version 1.17.1) and context jwst_1322.pmap from the calibration references data system (CRDS; see Peeters et al. (2024) for the observation parameters and data-reduction process). We used the average spectrum extracted over the apertures given by Berné et al. (2023). These spectra are in units of MJy sr^{-1}. A smooth spline function with a low spectral frequency continuum was subtracted for the comparison with the modeled spectrum.

Upon close inspection of JWST data of the disk, no obvious emission lines are detected close to the calculated CH_2^+ transitions (see Fig. 3). The typical line position accuracy of the calculations, based on the adopted potential surface, is expected to be better than a wavenumber. Thus, we derived an observational upper limit for the beam-averaged column density of vibrationally excited CH_2^+ in d203-506.

[2] `https://pdrs4all.org/`, DOI: 10.17909/pg4c-1737

The beam-averaged emission from an upper level is given by

$$J_u = \frac{h\,\nu_{ul}}{4\pi} A_{ul}\, N_u, \tag{4}$$

where h is the Planck constant, A_{ul} is the Einstein coefficient of the considered transition from upper (u) to lower (l) state, ν_{ul} is the frequency of the transition, and N_u is the column density of the upper level,

$$N_u = g_{ns}(u)\,[2J(u) + 1]\exp[-h\nu(u)/kT]/Q(T), \tag{5}$$

with $J(u)$ the total angular momentum, $g_{ns}(u)$ the nuclear spin statistics, $\nu(u)$ the energy of level u, and

$$Q(T) = \sum_i g_{ns}(i)\,[2J(i) + 1]\exp[-h\nu(i)/kT]. \tag{6}$$

To estimate the beam-averaged upper limit of an observation for the column density for a given excitation temperature, we interpolated our modeled spectrum after convolution with a Gaussian profile with a wavelength-dependent spectral resolution as reported for the MIRI/MRS instrument (Argyriou et al. 2023), on the observed JWST wavenumber grid. We then selected the channels (i.e., lines) in the modeled spectrum above a threshold of 0.1 after normalization of the modeled spectrum to its maximum, thus selecting bands in the spectrum that are expected to contribute most to the observed astronomical signal at the selected excitation temperature[3]. We then calculated the weighted $\chi^2(N) = \Sigma_i w(i)\times[I_{\rm obs}(i)-I^N_{\rm model}(i)]^2/\Sigma_i w(i)$, where N is the beam-averaged column density of the model, i runs over the spectral channels of the observed spectrum, and $w(i)$ is the weight of this channel, taken as the normalized flux of the modeled spectrum above the threshold value, so that brighter lines have a greater weight. When the modeled column density asymptotically goes to zero, the $\chi^2(N \to 0)$ asymptotically reaches the noise on the data in the absence of a detection. The upper limit of the column density is then derived when the χ^2 reaches three times this minimum χ^2 (i.e., three times the reduced χ^2) to provide the derived upper limit of the detection.

Fig. 3 shows a calculated LTE spectrum at 660 K with a column density corresponding to this conservative upper limit on the beam-averaged column density, plotted against the JWST observations in the 1100-400 cm^{-1} (~9.1–25 µm) range, which includes the ν_2 band region. This chosen temperature of 660 K corresponds to the excitation temperature observed for CH_3^+ in the disk (Berné et al. 2023; Changala et al. 2023).

Fig. 4 displays the upper limits, depending on the LTE excitation temperature, we derived. The upper limit varies with the assumed excitation temperature because the levels are more excited at higher temperatures, and thus, the lines are brighter. In addition, more lines can be produced, and the probability increases that the lines fall within a region of possible detection. Except for temperatures well below about 400 K, the upper limits fall below about 10^{11} cm^{-2}. To take the potential inaccuracies in the line positions in the model into account, we also made the same calculations using a Monte-Carlo randomization of the transitions around their calculated positions, adding a conservative ±2cm^{-1} deviation, that is, slightly higher than the expected accuracy of the model for the adopted potential energy surface. We calculated 1000 such randomization models for each temperature. The derived upper limits lying above the current adopted model are shown by a shaded area in Fig. 4. The boundary of the region thus represents the worst-case scenario for line positions with respect to the observed spectrum and is higher by about a factor of two than the current model.

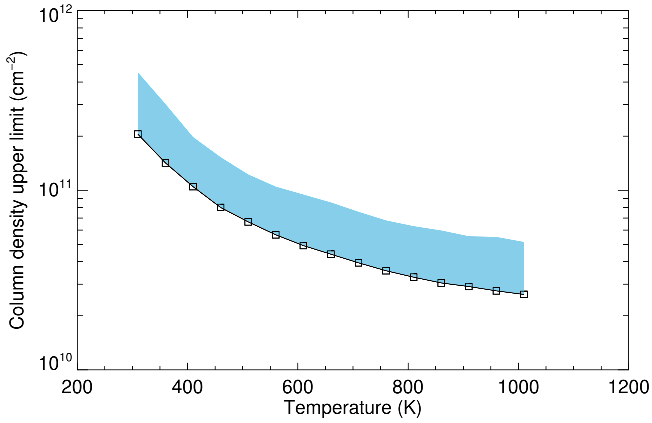

Fig. 4. Beam-averaged upper limits of the excited column density of CH_2^+ for the Orion disk d203-506 derived as a function of the excitation temperature for the calculated model (squares). The blue shaded area is the upper-limit region obtained by applying a Monte Carlo random shift position for each calculated transition (see Sect. 4 for details). The excited and non-excited column density in the emitting region is expected to be higher by about 100 times than these values.

5. PDR models

In this section, we present the results for our fiducial model, which is representative of the external layers of d203-506, from the Meudon PDR code (version 7.1[4], Le Petit et al. 2006) using similar parameters as for previous models of this source (Berné et al. 2023; Goicoechea et al. 2024, 2025b). We assumed an isochoric model with $n_{\rm H} = 10^7$ cm^{-3}. We adopted an incident UV field from an illuminating O7 star with an effective temperature $T_{\rm eff}$ = 40000 K modeled by a blackbody at $T_{\rm eff}$. The distance to the star was set so that the UV field intensity at the ionization front was equal to $G_0 = 2 \times 10^4$. We assumed the extinction curve toward HD38087 from Fitzpatrick & Massa (1990) with $R_V = 5.5$. We updated the photodissociation rate of CH_3^+ using del Mazo-Sevillano et al. (2024).

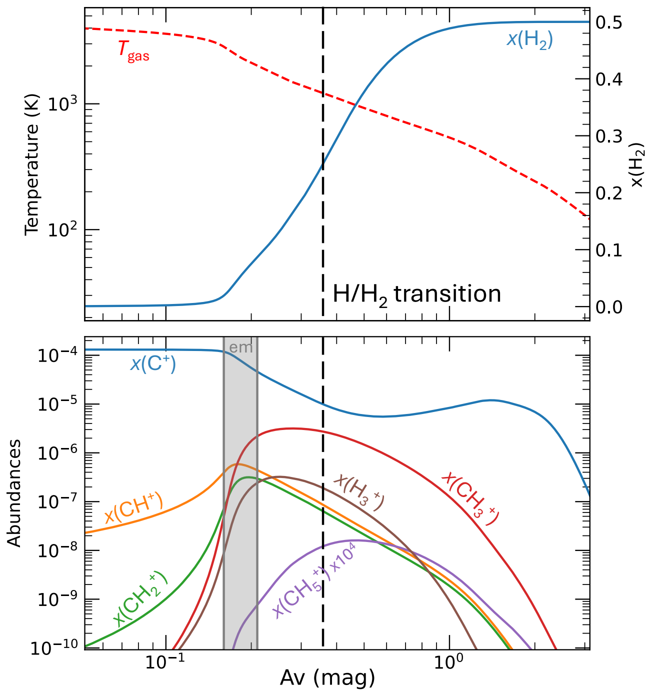

Fig. 5. Meudon PDR model at $n_{\rm H} = 10^7$ cm^{-3} and $G_0 = 2 \times 10^4$. (Top panel) Temperature and H_2 abundance profile as a function of A_V. (Bottom panel) Abundances with respect to the proton density of the main species of the carbon chemical chain. The gray area is defined as the emitting region of rovibrational levels of CH^+ and CH_3^+.

Figure 5 shows the temperature and abundance profile of the studied species as a function of depth inside the PDR (in units of extinction in the visible). This figure shows that CH^+, CH_2^+, and CH_3^+ peak at roughly the same position (near the H/H_2 transition, where $x(H_2) = 0.25$). This model predicts the CH_3^+

[3] In this method, we considered the lines independently, not in a stacking-like manner.
[4] Public version of November 2025: https://pdr.obspm.fr/pdr_download.html

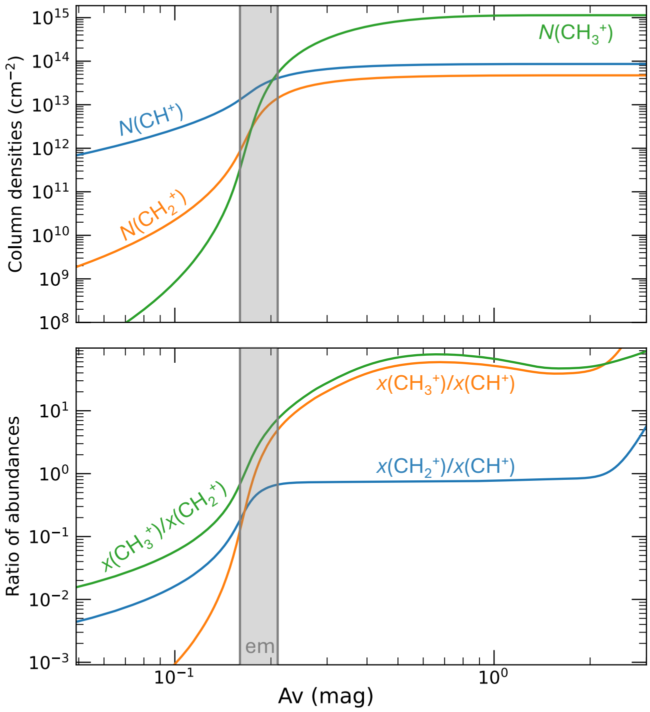

Fig. 6. Variation in the total column densities and abundances ratio of CH$^+$, CH$_2^+$, and CH$_3^+$ as a function of A_V for a model at $n_H = 10^7$ cm^{-3} and $G_0 = 2 \times 10^4$. The gray area is defined as the emitting region for rovibrational transitions of CH$^+$ and CH$_3^+$.

abundance to be higher by an order of magnitude than CH$^+$ and CH$_2^+$ at the dissociation front. CH$^+$ and CH$_2^+$ have a very similar abundance at this position, with CH$^+$ being slightly more abundant (by a factor of 2). Even though CH$^+$ peaks at the same position as CH$_2^+$ and CH$_3^+$, its abundance is higher closer to the edge of the PDR due to the need for excited H_2 to overcome the endothermicity of the C$^+$ + H_2 = CH$^+$ + H reaction. In contrast, the CH$_3^+$ abundance decreases more slowly deeper into the PDR because it is not efficiently destroyed by reactions with H_2 such as CH$^+$ and CH$_2^+$. Fig. 6 highlights these variations in morphology in the model by displaying the column density profiles and the variation in the abundance ratios as a function of A_V. Our fiducial model predicts $N(\mathrm{CH}^+) = 9.2 \times 10^{13}$ cm^{-2}, $N(\mathrm{CH}_2^+) = 5.3 \times 10^{13}$ cm^{-2}, and $N(\mathrm{CH}_3^+) = 1.1 \times 10^{15}$ cm^{-2}. Hence, the model predicts the column density of CH$_2^+$ to be twice lower than that of CH$^+$ and 20 times lower than that of CH$_3^+$. The fraction of excited species observed, in the case of CH$^+$ and CH$_3^+$, is lower than these predictions, but with similar column densities of $N(\mathrm{CH}^+) = (3.3 \pm 0.3) \times 10^{11}$ cm^{-2} and $N(\mathrm{CH}_3^+) = (5.4 \pm 3.2) \times 10^{11}$ cm^{-2} observed in the rovibrational states. This means that the column density ratio of the rovibrationally excited (observed) to total population (modeled) is different for CH$^+$ and CH$_3^+$, around 0.3% for CH$^+$ and 0.05% for CH$_3^+$. However, Fig. 5 reveals that CH$_3^+$ is more abundant at high A_V, at deeper positions than where the emission of rovibrational levels is expected to originate. The emitting region of rovibrational levels is expected around the abundance peak of CH$^+$ and CH$_3^+$. We can define the emitting region (later named "em", represented as the shaded area in Fig. 5 and 6) where the abundance of CH$^+$ is at least 75% of its maximum abundance, which corresponds to $A_V = 0.16 - 0.21$. Then, in this region $N_{\mathrm{em}}(\mathrm{CH}^+) \sim 3 \times 10^{13}$ cm^{-2} and $N_{\mathrm{em}}(\mathrm{CH}_3^+) \sim 6 \times 10^{13}$ cm^{-2}. The fraction of excited levels is similar and about 1%. Hence, we also expect that for d203-506, the column density of rovibrational levels of CH$_2^+$ is about 1% of its column density at low A_V. In the fiducial model, $N_{\mathrm{em}}(\mathrm{CH}_2^+) \sim 1.5 \times 10^{13}$ cm^{-2}, so we expect $N_{\mathrm{exc}}(\mathrm{CH}_2^+) \sim 1.5 \times 10^{11}$ cm^{-2}. In the emitting region, the column density of these species varies drastically (see Fig. 6). The percentage of the excited column density might therefore be lower or higher than 1% and should be treated as a rough estimate.

Depending on the underlying excitation temperature, this is above or just below the upper limit we inferred from the comparison to JWST spectra shown in Fig. 4. If CH$_2^+$ has an equivalent excitation temperature of about 600 K as observed for CH$_3^+$, we should still see hints of detection of some well-isolated transitions at this level, such as the doublet around 1025 cm^{-1} (see Fig. 3). These models suggest that pushing the JWST integration time might reveal the presence of CH$_2^+$, as it currently seems to be at the detection limit.

6. Discussion

6.1. Detection of CH$_2^+$

Since it is a very reactive intermediate in the ion reaction network, CH$_2^+$ is difficult to observe. Nevertheless, constraining its abundance provides insight into chemical networks, as models expect it to be only several times less abundant than CH$_3^+$ and CH$^+$ in peak excitation regions. Assuming its excitation temperature to be of the same order as the one observed for most species detected in the near- and mid-IR in the Orion Bar with JWST, spanning the 600-1000 K range for most of them, we estimated a CH$_2^+$ excited column density upper limit that is lower by about one order of magnitude than the one detected for CH$_3^+$. We also provide a list of transitions for calculating CH$_2^+$ spectra and for hopefully obtaining a detection or more constraining upper limits from future observations, thus providing constraints for astrochemical models. Regions that therefore should favor CH$_2^+$ are those in which it is less efficiently destroyed, that is, those with a relatively low H_2 density (but still high enough for it to form), short dynamical timescales, and a high ionization fraction. Conversely, regions that favor CH$_3^+$ include a higher abundance of H_2 and higher densities, which would increase the efficiency of the carbocation reaction chain, described in reactions (1), (2). This difference in required conditions is observed in PDR models, where the CH$_3^+$/CH$_2^+$ ratio decouples at moderate A_V (see Fig. 6). In addition, CH$_3^+$ has a lower electronic recombination efficiency, and thus, quasi-stationary conditions will favor it. When CH$^+$ is formed, conversion into CH$_2^+$ by interaction with H_2 is rapid and exothermic. Then, it proceeds rapidly to form CH$_3^+$ and CH$_3^+$ appears as the relaxed product of any injection of CH$^+$, CH$_2^+$ being an intermediate. The ratios CH$^+$/CH$_2^+$/CH$_3^+$ should therefore measure the equilibrium between energy injection (endoergic formation for CH$^+$) and chemical relaxation (hydrogenation towards CH$_3^+$), which makes them direct tracers of out-of-equilibrium energetic dissipation of energy in interstellar gas.

6.2. The H_2 + CH$^+$ $\longrightarrow$ CH$_2^+(\widetilde{X},\widetilde{A})$ +H formation reaction

A deepest understanding of CH$_2^+$ formation pathways is required, in addition to its spectroscopic properties, to assess whether the nondetection of CH$_2^+$ is compatible with current predictions by astrochemical models. First, it is important to determine the population distribution of the CH$_2^+$ energy levels following its formation via H_2 + CH$^+$, which might deviate from an LTE-like

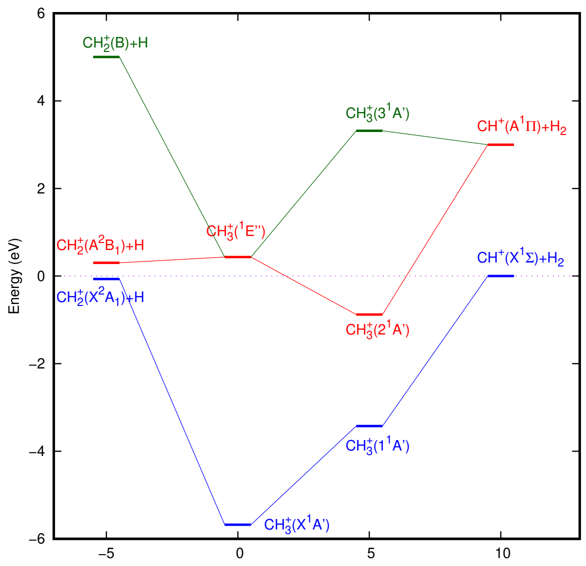

Fig. 7. Energy diagram of the lower electronic states involved in the H_2 + CH^+ ⟶ CH_2^+ + H reaction from del Mazo-Sevillano et al. (2024) , including zeropoint energies.

distribution at temperatures lower than 1000 K. CH_2^+ might also be formed in very excited ν_2 levels in the $\tilde{X}$ state or even in its first electronic excited state ($\tilde{A}^+$).

The reaction

$$CH^+(X^1\Sigma) + H_2(X^1\Sigma^+) \rightarrow CH_2^+(\widetilde{X}^2A_1, \widetilde{A}^2B_1) + H(^2S) \qquad (7)$$

proceeds through the formation of the $CH_3^+(\widetilde{X}^1A')$ system and is slightly exothermic. The ground and first two excited electronic states of the full CH_3^+ system were calculated recently for the study of $CH_3^+(\widetilde{X}^1A')$ photodissociation (del Mazo-Sevillano et al. 2024), and the energy diagram with some stationary points (including zeropoint energy) is shown in Fig. 7. Clearly, the $CH_2^+(\widetilde{X}^2A_1)$ correlates adiabatically with the reactants, in a reaction that is exothermic by only ≈ 66 meV, using the explicitly correlated internally contracted multireference configuration interaction (ic-MRCI-F12) method (Werner & Knowles 1988; Shiozaki & Werner 2011), with the MOLPRO suite of programs (Werner et al. 2012) and the cc-pCVTZ-F12 electronic basis set (Hill et al. 2010).

In contrast, the formation of the excited $CH_2^+(\widetilde{A}^2B_1)$ products correlates with the electronically excited $CH^+(A^1\Pi)$. Transitions among these two electronic states are negligible along the reaction path until they form the CH_2^+ products, where the energy separation is significantly reduced. The symmetry of the two electronic states of CH_2^+ is different, and they are only coupled by the weak spin-orbit and electronic Coriolis force, which cause the Renner-Teller effects. These couplings are important for accurately describing the spectroscopy of the ions, but they are rather small, so the electronic transitions between them can be neglected. Moreover, the reaction to form excited $CH_2^+(\widetilde{A}^2B_1)$ is endothermic by ≈ 303 meV, so that at low temperatures, this reactive channel is unreachable.

In summary, in the H_2 + CH^+ reaction mainly $CH_2^+(\widetilde{X})$ is expected to be formed, following a statistical mechanism discussed in Appendix A, with a rate of 1.01 10^{-9} $(T/300)^{-0.193}$ exp(-16.0/T) cm^3s^{-1} for $20 < T < 1000$ K. In the KIDA database, a constant value of 1.20 10^{-9} cm^3s^{-1} is reported, based on a estimation by Anicich (1993). Because of the statistical mechanism, the $CH_2^+(\widetilde{X})$ is expected to be formed with a rovibrational population following a Boltzmann distribution.

6.3. Importance of transitions from the $\tilde{A}^+$ level

If $CH_2^+(\widetilde{A})$ is only a minor product in the reaction CH^+ + H_2, it can be formed in this excited electronic state through alternative routes. One of these routes is the photodissociation of $CH_3^+(\widetilde{X})$, as recently reported by del Mazo-Sevillano et al. (2024) and displayed in the energy diagram of Fig. 7. If this route becomes important, CH_2^+ might deexcite through a vibrational transition from its least energetic vibrational mode ($\nu_2 = 1 \rightarrow \nu_2 = 0$ in $\tilde{A}^+$), which is expected around 2500 cm^{-1} (∼ 4 μm). Alternatively, it might relax to its ground electronic state ($\tilde{X}^+$) via vibronic emission. As demonstrated by Wang et al. (2013), the large change in geometry between the $\tilde{X}^+$ and $\tilde{A}^+$ states implies a strong nondiagonal Franck-Condon progression along the ν_2 vibrational mode in the $\tilde{A}^+ \leftarrow \tilde{X}^+$ absorption spectrum of CH_2^+. The emission spectrum from $\tilde{A}^+$ state toward $\tilde{X}^+$ will thus also present a long vibrational progression, but at a lower frequency (or higher wavelength). If only the first vibrational levels of the $\tilde{A}^+$ state are populated, based on the CH^+ and CH_3^+ excitation temperatures in the different objects in which it was detected (between 700 and 1500 K), the strongest emission transitions will be toward the excited vibrational levels of $\tilde{X}^+$. We would then expect emission features of CH_2^+ from the $\nu_2 = 0$ and $\nu_2 = 1$ of the $\tilde{A}^+$ electronic state toward the ν_2 bending levels of the $\tilde{X}^+$ electronic state. The expected ranges for such transitions are reported in Fig 2. Typical vibronic emissions present a higher probability than vibrational emissions, and CH_2^+ spectroscopic signatures might therefore be spread (large number of transitions) and contribute to other spectral regions. The emission spectrum of CH_2^+ in hot environments might even be located in the near-IR region, especially if CH_2^+ is produced in vibrational states higher than ν_2=1 in the $\tilde{A}^+$ electronic state. Further investigation of CH_2^+ formation pathways and degree of excitation is thus required.

7. Conclusion

We investigated the observational conditions required to constrain the presence of the particularly hard-to-detect CH_2^+ reactive species. We calculated and identified mid- and far-IR transitions expected to be most relevant, with an emphasis on low-lying rovibrational states. Synthetic emission spectra were produced for a range of excitation temperatures and compared with observations of the irradiated disk d203-506, in which chemically related species are known to be present. The main conclusions of this study are summarized below

1. We derived observationally temperature-dependent upper limits on the CH_2^+ excited column density for the irradiated disk d203-506, which were found to be significantly lower (about an order of magnitude) than the column densities measured for other carbocations in excited states.
2. Using a fiducial PDR model of d203-506, we showed that CH^+, CH_2^+, and CH_3^+ are expected to originate from the same region, near the H/H_2 transition, and to have very similar abundances.
3. This model predicts that the column density of rovibrational levels of CH^+ and CH_3^+ only represents 1% of their column density in the emitting region. Assuming that CH_2^+ follows the same logic, we predict a column density that is consistent with its nondetection in d203-506.

4. The CH_3^+ and CH_2^+ ratio is expected to decouple at moderate A_V, which indicates that the regions that are expected to favor CH_2^+ are those with a relatively low H_2 density, short dynamical timescales, and a high ionization fraction. The ratios $CH^+/CH_2^+/CH_3^+$ are expected to measure the equilibrium between energy injection and chemical relaxation.

Future laboratory measurements are essential for benchmarking and refining the theoretical predictions. While we await these laboratory experiments to evaluate the accuracy of the calculations, and thus, to refine the astronomical search for CH_2^+, we present a comprehensive set of tabulated transitions to support future observational searches for this carbocation. These data will facilitate either direct detections or the derivation of more stringent upper limits, thereby providing critical benchmarks for astrochemical models, particularly in photon-dominated environments.

Acknowledgements.
This work is based [in part] on observations made with the NASA/ESA/CSA James Webb Space Telescope. The data were obtained from the Mikulski Archive for Space Telescopes at the Space Telescope Science Institute, which is operated by the Association of Universities for Research in Astronomy, Inc., under NASA contract NAS 5-03127 for JWST. These observations are associated with program #1288 (DOI: 10.17909/pg4c-1737). Support for program #1288 was provided by NASA through a grant from the Space Telescope Science Institute, which is operated by the Association of Universities for Research in Astronomy, Inc., under NASA contract NAS 5-03127, and the Canadian Space Agency (CSA, 22JWGO1-16). This work was performed in part at the French MIRI center with the support of CNES and the ANR-labcom INCLASS between IAS and ACRI-ST, and also supported by the Program National "Physique et Chimie du Milieu Interstellaire" (PCMI) of CNRS/INSU with INC/INP cofunded by CEA and CNES. M.Z. and J.R.G. thank the Spanish MCINN for funding support under grant PID2023-146667NB-I00. M. Z. acknowledges the Juan de la Cierva Postdoctoral Fellow project JDC2024-054658-I, funded by MICIU/AEI/10.13039/501100011033 and by the ESF+. O.R. and P.dM-D thank Spanish MCINN for funding support under grant PID2024-156686NB-I00. E.P. and J.C. acknowledge support from the University of Western Ontario, the Institute for Earth and Space Exploration, the Canadian Space Agency (CSA, 22JWGO1-16), and the Natural Sciences and Engineering Research Council of Canada. C.B. acknowledges support from the Internal Scientist Funding Model (ISFM) Laboratory Astrophysics Directed Work Package Round 3 at NASA Ames and is grateful for an appointment at NASA Ames Research Center through the San José State University Research Foundation (80NSSC22M0107).

References

Anicich, V. G. 1993, Journal of Physical and Chemical Reference Data, 22, 1469
Argyriou, I., Glasse, A., Law, D. R., et al. 2023, A&A, 675, A111
Berné, O., Habart, É., Peeters, E., et al. 2022, PASP, 134, 054301
Berné, O., Martin-Drumel, M.-A., Schroetter, I., et al. 2023, Nature, 621, 56
Bhatt, C., Cami, J., Peeters, E., et al. 2025, ApJ, 995, 67
Bruderer, S., Benz, A. O., van Dishoeck, E. F., et al. 2010, A&A, 521, L44
Bunker, P., Chan, M., Kraemer, W., & Jensen, P. 2001, Chemical physics letters, 341, 358
Bunker, P., Kraemer, W. P., Yurchenko, S. N., et al. 2007, Molecular Physics, 105, 1369
Carter, S. & Handy, N. C. 1982, Journal of Molecular Spectroscopy, 95, 9
Cernicharo, J., Liu, X. W., González-Alfonso, E., et al. 1997, ApJ, 483, L65
Changala, P. B., Chen, N. L., Le, H. L., et al. 2023, A&A, 680, A19
Coudert, L. H., Gans, B., Holzmeier, F., et al. 2018, The Journal of Chemical Physics, 149, 224304
del Mazo-Sevillano, P. d., Aguado, A., Goicoechea, J. R., & Roncero, O. 2024, J. Chem. Phys., 160, 184307
Douglas, A. E. & Herzberg, G. 1941, ApJ, 94, 381
Falgarone, E., Godard, B., Cernicharo, J., et al. 2010, A&A, 521, L15
Fitzpatrick, E. L. & Massa, D. 1990, ApJS, 72, 163
Geballe, T. R. 2006, Philosophical Transactions of the Royal Society of London Series A, 364, 3035
Geballe, T. R. & Oka, T. 1996, Nature, 384, 334
Goicoechea, J. R., Le Bourlot, J., Black, J. H., et al. 2024, A&A, 689, L4
Goicoechea, J. R., Pety, J., Cuadrado, S., et al. 2025a, A&A, 696, A100
Goicoechea, J. R., Roncero, O., Roueff, E., et al. 2025b, A&A, 703, A189
Goto, M., Usuda, T., Nagata, T., et al. 2008, ApJ, 688, 306
Gottfried, J. L. & Oka, T. 2004, The Journal of chemical physics, 121, 11527
Gutlé, C. & Coudert, L. H. 2012, Journal of Molecular Spectroscopy, 273, 44
Henning, T., Kamp, I., Samland, M., et al. 2024, PASP, 136, 054302
Herbst, E. 2021, Frontiers in Astronomy and Space Sciences, 8, 207
Herzberg, G. 1966, Molecular Spectra and Molecular Structure. Vol. III: Electronic Spectra and Electronic Structure of Polyatomic Molecules (Princeton, NJ / New York, USA: D. Van Nostrand Company), volume III of *Molecular Spectra and Molecular Structure*
Hill, J. G., Mazumder, S., & Peterson, K. A. 2010, The Journal of chemical physics, 132
Indriolo, N. & McCall, B. J. 2012, ApJ, 745, 91
Indriolo, N., Oka, T., Geballe, T. R., & McCall, B. J. 2010, ApJ, 711, 1338
Jensen, P., Brumm, M., Kraemer, W., & Bunker, P. 1995a, Journal of Molecular Spectroscopy, 172, 194
Jensen, P., Brumm, M., Kraemer, W. P., & Bunker, P. R. 1995b, Journal of Molecular Spectroscopy, 171, 31
Jungen, C. 2019, Journal of Molecular Spectroscopy, 363, 111172
Kraemer, W., Jensen, P., & Bunker, P. 1994, Canadian Journal of Physics, 72, 871
Le Petit, F., Nehmé, C., Le Bourlot, J., & Roueff, E. 2006, ApJS, 164, 506
Marcus, R. A. 1952a, J. Chem. Phys., 20, 352
Marcus, R. A. 1952b, J. Chem. Phys., 20, 355
McCall, B. J., Hinkle, K. H., Geballe, T. R., et al. 2002, ApJ, 567, 391
Miller, W. H. 1987, Chem. Rev., 87, 19
Morris, P. W., Gupta, H., Nagy, Z., et al. 2016, ApJ, 829, 15
Naylor, D. A., Dartois, E., Habart, E., et al. 2010, A&A, 518, L117
Osmann, G., Bunker, P. R., Jensen, P., & Kraemer, W. P. 1997, Chemical Physics, 225, 33
Peeters, E., Habart, E., Berné, O., et al. 2024, A&Ap, 685, A74
Rangwala, N., Maloney, P. R., Glenn, J., et al. 2014, ApJ, 788, 147
Reuter, W. & Peyerimhoff, S. D. 1992, Chemical Physics, 160, 11
Rösslein, M., Gabrys, C., Jagod, M.-F., & Oka, T. 1992, Journal of molecular spectroscopy, 153, 738
Shiozaki, T. & Werner, H.-J. 2011, The Journal of chemical physics, 134
Smith, D. 1992, Chemical Reviews, 92, 1473
Solomonik, V. & Yachmenev, A. Y. 2008, Optics and Spectroscopy, 104, 818
Spinoglio, L., Pereira-Santaella, M., Busquet, G., et al. 2012, ApJ, 758, 108
Thi, W. F., Ménard, F., Meeus, G., et al. 2011, A&A, 530, L2
Volz, M., Espaillat, C. C., Pittman, C. V., et al. 2026, AJ, 171, 39
W. H. Miller. 1979, J. Am. Chem. Soc., 101
Wang, H., Neese, C. F., Morong, C. P., Kleshcheva, M., & Oka, T. 2013, Journal of Physical Chemistry A, 117, 9908
Werner, H., Knowles, P., Knizia, G., Manby, F., & Schütz, M. 2012, Mol. Sci, 2, 10
Werner, H.-J. & Knowles, P. J. 1988, J. Chem. Phys., 89, 5803
Wesson, R., Cernicharo, J., Barlow, M. J., et al. 2010, A&A, 518, L144
Willitsch, S. & Merkt, F. 2003, The Journal of chemical physics, 118, 2235
Woon, D. E. & Herbst, E. 2009, ApJ. Sup. Series, 185, 273
Zannese, M., Tabone, B., Habart, E., et al. 2025, A&A, 696, A99
Zannese, M., Tabone, B., Habart, E., et al. 2024, Nature Astronomy, 8, 577

Appendix A: $CH_2^+(\widetilde{X})$ formation rate

The ground state potential is attractive between CH^+ and H_2, with no barrier to form CH_3^+, so that the reaction takes place through the formation of long-lived $(CH_3^+)^*$ complexes, followed by the dissociation of the complex either towards $CH^+ + H_2$ or to $CH_2^+(\widetilde{X})$ + H, channels.

The $CH^+ + H_2 \longrightarrow CH_2^+(\widetilde{X})$ + H micro-canonical reaction rate constant is given by

$$K(E) = \sigma_c(E) \frac{K_{CH_2^+ + H}(E)}{K_{CH_2^+ + H}(E) + K_{CH^+ + H_2}(E)} \quad \text{(A.1)}$$

The capture cross section, $\sigma_c(T) = \pi\sqrt{e^2 2\alpha/E_t}$ for the formation of these complexes is dominated by the charge-induced electric dipole long-range interaction, giving a Langevin rate for hydrogen molecule of 2.25 10^{-9} $cm^3 s^{-1}$ using the H_2 polarizability of Woon & Herbst (2009).

The unimolecular dissociation rate constants are calculated using the statistical RRKM theory (Marcus 1952a,b). The microcanonical rate constants to dissociate the $(CH_3^+)^*$ complex are evaluated towards each re-arrangement channel α ($CH^+ + H_2$ or CH_2^+ + H) independently at each total energy E and total angular momentum J as (Marcus 1952a,b; W. H. Miller 1979; Miller 1987)

$$K_\alpha(E, J) = \frac{\sum_{q,\ell} P(E, J, q, \ell)}{2\pi\hbar\rho(E, J)} \quad \text{(A.2)}$$

where $q = v_A, v_B, J_A, J_B, K_A, K_B$ denotes the quantum numbers defining the states of fragments A and B, with eigenvalues ϵ_q and $\rho(E, J)$ is the density of states of the $(CH_3^+)^*$ complex. In the above expression, the probability is evaluated classically as $P(E, J, q, \ell) = 1$ for $E > E^b_{q\ell}$ (and zero elsewhere), with $E^b_{q\ell}$ being the rotational barrier. In all these expressions, the rovibrational eigenvalues are evaluated in a rigid rotor approximation of harmonic oscillators for H^+, H_2 , CH_2^+ and CH_3^+ at their corresponding equilibrium geometries. The corresponding reaction rate of Eq. A.1 is then integrated numerically to obtain the thermal reaction rate constant reported in section 6.2.

Appendix B: Calculated tables of levels

Table B.1 shows a small portion of the level list computed in Section 3.

Table B.1. A portion of the levels computed in Section 3.

$N_{K_aK_c}$	F_{12}	v	L	Γ	E(cm^{-1})	g
0_{00}	F_1	(000)	$\tilde{X}^+$	A_1	0.000	1
1_{01}	F_2	(000)	$\tilde{X}^+$	B_1	14.692	3
1_{01}	F_1	(000)	$\tilde{X}^+$	B_1	14.692	3
2_{02}	F_2	(000)	$\tilde{X}^+$	A_1	44.062	1
2_{02}	F_1	(000)	$\tilde{X}^+$	A_1	44.062	1
1_{10}	F_2	(000)	$\tilde{X}^+$	A_2	74.694	1
1_{11}	F_2	(000)	$\tilde{X}^+$	B_2	75.528	3
1_{11}	F_1	(000)	$\tilde{X}^+$	A_2	77.113	1
1_{10}	F_1	(000)	$\tilde{X}^+$	B_2	77.951	3
3_{03}	F_2	(000)	$\tilde{X}^+$	B_1	88.082	3
3_{03}	F_1	(000)	$\tilde{X}^+$	B_1	88.082	3
2_{11}	F_2	(000)	$\tilde{X}^+$	B_2	104.064	3
2_{11}	F_1	(000)	$\tilde{X}^+$	B_2	105.395	3
2_{12}	F_2	(000)	$\tilde{X}^+$	A_2	106.567	1
2_{12}	F_1	(000)	$\tilde{X}^+$	A_2	107.904	1
3_{12}	F_2	(000)	$\tilde{X}^+$	A_2	147.127	1
3_{13}	F_1	(000)	$\tilde{X}^+$	A_2	148.058	1
3_{13}	F_2	(000)	$\tilde{X}^+$	B_2	152.126	3
3_{12}	F_1	(000)	$\tilde{X}^+$	B_2	153.065	3
2_{20}	F_2	(000)	$\tilde{X}^+$	B_1	310.574	3
2_{21}	F_2	(000)	$\tilde{X}^+$	A_1	310.581	1
2_{20}	F_1	(000)	$\tilde{X}^+$	B_1	313.774	3
2_{21}	F_1	(000)	$\tilde{X}^+$	A_1	313.781	1
3_{22}	F_2	(000)	$\tilde{X}^+$	A_1	355.508	1
3_{21}	F_2	(000)	$\tilde{X}^+$	B_1	355.543	3
3_{22}	F_1	(000)	$\tilde{X}^+$	A_1	357.746	1
3_{21}	F_1	(000)	$\tilde{X}^+$	B_1	357.781	3
3_{31}	F_2	(000)	$\tilde{X}^+$	B_2	649.744	3
3_{30}	F_2	(000)	$\tilde{X}^+$	A_2	649.744	1
3_{31}	F_1	(000)	$\tilde{X}^+$	A_2	653.263	1
3_{30}	F_1	(000)	$\tilde{X}^+$	B_2	653.264	3
1_{10}	F_2	(010)	$\tilde{X}^+$	A_2	956.121	1
1_{11}	F_2	(010)	$\tilde{X}^+$	B_2	956.829	3
1_{10}	F_1	(010)	$\tilde{X}^+$	A_2	966.662	1
1_{11}	F_1	(010)	$\tilde{X}^+$	B_2	967.382	3
2_{12}	F_2	(010)	$\tilde{X}^+$	B_2	987.859	3
2_{11}	F_2	(010)	$\tilde{X}^+$	A_2	989.990	1
2_{11}	F_1	(010)	$\tilde{X}^+$	B_2	993.698	3
0_{00}	F_1	(010)	$\tilde{X}^+$	A_1	995.655	1
2_{12}	F_1	(010)	$\tilde{X}^+$	A_2	995.848	1
1_{01}	F_1	(010)	$\tilde{X}^+$	B_1	1010.339	3
1_{01}	F_2	(010)	$\tilde{X}^+$	B_1	1010.339	3
3_{13}	F_2	(010)	$\tilde{X}^+$	A_2	1031.304	1
3_{12}	F_1	(010)	$\tilde{X}^+$	A_2	1035.392	1
3_{12}	F_2	(010)	$\tilde{X}^+$	B_2	1035.562	3
3_{13}	F_1	(010)	$\tilde{X}^+$	B_2	1039.676	3
2_{02}	F_1	(010)	$\tilde{X}^+$	A_1	1039.695	1
2_{02}	F_2	(010)	$\tilde{X}^+$	A_1	1039.695	1
3_{03}	F_2	(010)	$\tilde{X}^+$	B_1	1083.697	3
3_{03}	F_1	(010)	$\tilde{X}^+$	B_1	1083.698	3

Notes. Levels are assigned using rotational quantum numbers $N_{K_aK_c}$, the electron spin-rotation label F_{12}, the vibrational quantum numbers $v = (v_1v_2v_3)$, the electronic state label L, and their C_{2v} symmetry Γ. Energies in cm^{-1} and nuclear spin statistical weights are given in the column headed E and g, respectively.

Appendix C: Calculations details

Table C.1 shows a small portion of line list calculated in Section 3.

Table C.1. A portion of the transitions computed in Section 3.

Upper level				Lower level						
$N_{K_aK_c}$	F_{12}	v	L	$N_{K_aK_c}$	F_{12}	v	L	ν	S	A_{12}
3_{13}	F_1	(000)	$\tilde{X}^+$	4_{04}	F_1	(000)	$\tilde{X}^+$	1.34912	0.702787e+0	0.676538e−7
4_{14}	F_1	(010)	$\tilde{X}^+$	3_{03}	F_1	(010)	$\tilde{X}^+$	7.69236	0.800667e+0	0.114297e−4
2_{02}	F_2	(010)	$\tilde{X}^+$	3_{13}	F_2	(010)	$\tilde{X}^+$	8.39151	0.457150e+0	0.211798e−4
5_{05}	F_2	(000)	$\tilde{X}^+$	4_{13}	F_1	(000)	$\tilde{X}^+$	14.88201	0.173483e−1	0.179326e−5
5_{05}	F_1	(000)	$\tilde{X}^+$	4_{13}	F_1	(000)	$\tilde{X}^+$	14.88329	0.936534e+0	0.806940e−4
5_{05}	F_2	(000)	$\tilde{X}^+$	4_{14}	F_2	(000)	$\tilde{X}^+$	15.60108	0.762806e+0	0.908406e−4
2_{11}	F_2	(000)	$\tilde{X}^+$	3_{03}	F_2	(000)	$\tilde{X}^+$	15.98245	0.331877e+0	0.106230e−3
1_{01}	F_1	(010)	$\tilde{X}^+$	2_{11}	F_1	(010)	$\tilde{X}^+$	16.64143	0.516600e+0	0.186667e−3
5_{14}	F_2	(010)	$\tilde{X}^+$	4_{04}	F_2	(010)	$\tilde{X}^+$	16.67777	0.770687e+0	0.112123e−3
2_{11}	F_1	(000)	$\tilde{X}^+$	3_{03}	F_1	(000)	$\tilde{X}^+$	17.31330	0.474594e+0	0.128740e−3
2_{11}	F_1	(000)	$\tilde{X}^+$	3_{03}	F_2	(000)	$\tilde{X}^+$	17.31360	0.237352e−1	0.643882e−5
5_{14}	F_1	(010)	$\tilde{X}^+$	4_{04}	F_1	(010)	$\tilde{X}^+$	19.25375	0.948850e+0	0.176996e−3
1_{01}	F_2	(010)	$\tilde{X}^+$	2_{12}	F_2	(010)	$\tilde{X}^+$	22.48053	0.284793e+0	0.507365e−3
1_{01}	F_1	(010)	$\tilde{X}^+$	2_{12}	F_2	(010)	$\tilde{X}^+$	22.48056	0.569585e−1	0.507366e−4
0_{00}	F_1	(010)	$\tilde{X}^+$	1_{10}	F_1	(010)	$\tilde{X}^+$	28.99229	0.383520e+0	0.146557e−2
1_{10}	F_2	(000)	$\tilde{X}^+$	2_{02}	F_2	(000)	$\tilde{X}^+$	30.63176	0.136422e+0	0.614854e−3
1_{11}	F_1	(000)	$\tilde{X}^+$	2_{02}	F_1	(000)	$\tilde{X}^+$	33.05039	0.246066e+0	0.696504e−3
1_{11}	F_1	(000)	$\tilde{X}^+$	2_{02}	F_2	(000)	$\tilde{X}^+$	33.05048	0.273463e−1	0.774058e−4
0_{00}	F_1	(010)	$\tilde{X}^+$	1_{10}	F_2	(010)	$\tilde{X}^+$	39.53374	0.189105e+0	0.183223e−2
1_{01}	F_2	(010)	$\tilde{X}^+$	1_{11}	F_1	(010)	$\tilde{X}^+$	42.95749	0.958427e−1	0.119137e−2
1_{01}	F_1	(010)	$\tilde{X}^+$	1_{11}	F_1	(010)	$\tilde{X}^+$	42.95752	0.479213e+0	0.297844e−2
5_{05}	F_2	(010)	$\tilde{X}^+$	5_{15}	F_1	(010)	$\tilde{X}^+$	43.30037	0.248162e−1	0.631847e−4
5_{05}	F_1	(010)	$\tilde{X}^+$	5_{15}	F_1	(010)	$\tilde{X}^+$	43.30358	0.161381e+1	0.342486e−2
4_{04}	F_2	(010)	$\tilde{X}^+$	4_{13}	F_1	(010)	$\tilde{X}^+$	43.80653	0.308765e−1	0.101755e−3
4_{04}	F_1	(010)	$\tilde{X}^+$	4_{13}	F_1	(010)	$\tilde{X}^+$	43.80824	0.135906e+1	0.358350e−2
2_{02}	F_2	(010)	$\tilde{X}^+$	2_{12}	F_1	(010)	$\tilde{X}^+$	43.84737	0.570185e−1	0.376867e−3
2_{02}	F_1	(010)	$\tilde{X}^+$	2_{12}	F_1	(010)	$\tilde{X}^+$	43.84762	0.798375e+0	0.351800e−2
3_{03}	F_2	(010)	$\tilde{X}^+$	3_{13}	F_1	(010)	$\tilde{X}^+$	44.02068	0.402743e−1	0.179576e−3
3_{03}	F_1	(010)	$\tilde{X}^+$	3_{13}	F_1	(010)	$\tilde{X}^+$	44.02145	0.108768e+1	0.363754e−2
5_{05}	F_2	(010)	$\tilde{X}^+$	5_{15}	F_2	(010)	$\tilde{X}^+$	45.91836	0.133548e+1	0.405507e−2
5_{05}	F_1	(010)	$\tilde{X}^+$	5_{15}	F_2	(010)	$\tilde{X}^+$	45.92157	0.247426e−1	0.626205e−4
4_{04}	F_2	(010)	$\tilde{X}^+$	4_{13}	F_2	(010)	$\tilde{X}^+$	46.99745	0.107614e+1	0.437930e−2
4_{04}	F_1	(010)	$\tilde{X}^+$	4_{13}	F_2	(010)	$\tilde{X}^+$	46.99917	0.307581e−1	0.100145e−3
3_{03}	F_2	(010)	$\tilde{X}^+$	3_{12}	F_2	(010)	$\tilde{X}^+$	48.13497	0.801116e+0	0.467012e−2
3_{03}	F_1	(010)	$\tilde{X}^+$	3_{12}	F_2	(010)	$\tilde{X}^+$	48.13573	0.400660e−1	0.175183e−3
2_{02}	F_2	(010)	$\tilde{X}^+$	2_{11}	F_2	(010)	$\tilde{X}^+$	49.70498	0.509200e+0	0.490264e−2
2_{02}	F_1	(010)	$\tilde{X}^+$	2_{11}	F_2	(010)	$\tilde{X}^+$	49.70522	0.565860e−1	0.363216e−3
1_{01}	F_2	(010)	$\tilde{X}^+$	1_{11}	F_2	(010)	$\tilde{X}^+$	53.51002	0.189025e+0	0.454147e−2
1_{01}	F_1	(010)	$\tilde{X}^+$	1_{11}	F_2	(010)	$\tilde{X}^+$	53.51005	0.945124e−1	0.113537e−2

Notes. Transitions are assigned using the rotational quantum numbers $N_{K_aK_c}$, the electron spin-rotation label F_{12}, the vibrational quantum numbers $v = (v_1 v_2 v_3)$, and the electronic state label L of the upper and lower levels. The transition frequency ν in cm^{-1}, the line strength S in Debye^2, and the Einstein coefficient A_{12} in s^{-1} are given.

Appendix D: Models comparisons in the 410-1010 K range

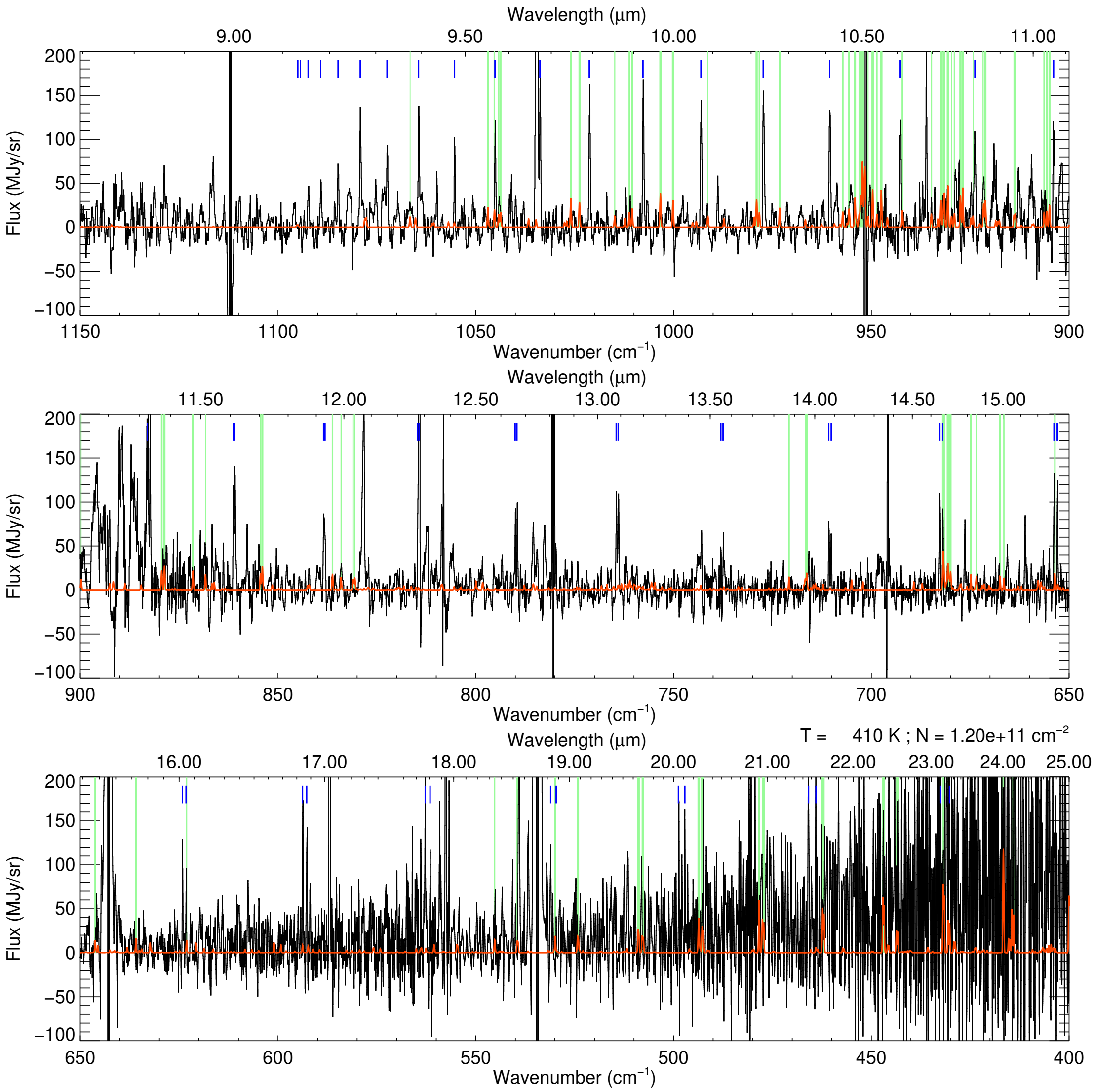

Fig. D.1. Comparison of the irradiated disk d203-506 continuum subtracted JWST spectrum to the CH_2^+ calculated LTE spectrum at 410 K with a column density limit corresponding to 1.2×10^{11} cm^{-2} (red). The series of emission lines labeled with blue vertical marks corresponds to OH emission already reported in The vertical green regions indicate the CH_2^+ lines used to constrain the upper limit derived at that excitation temperature.

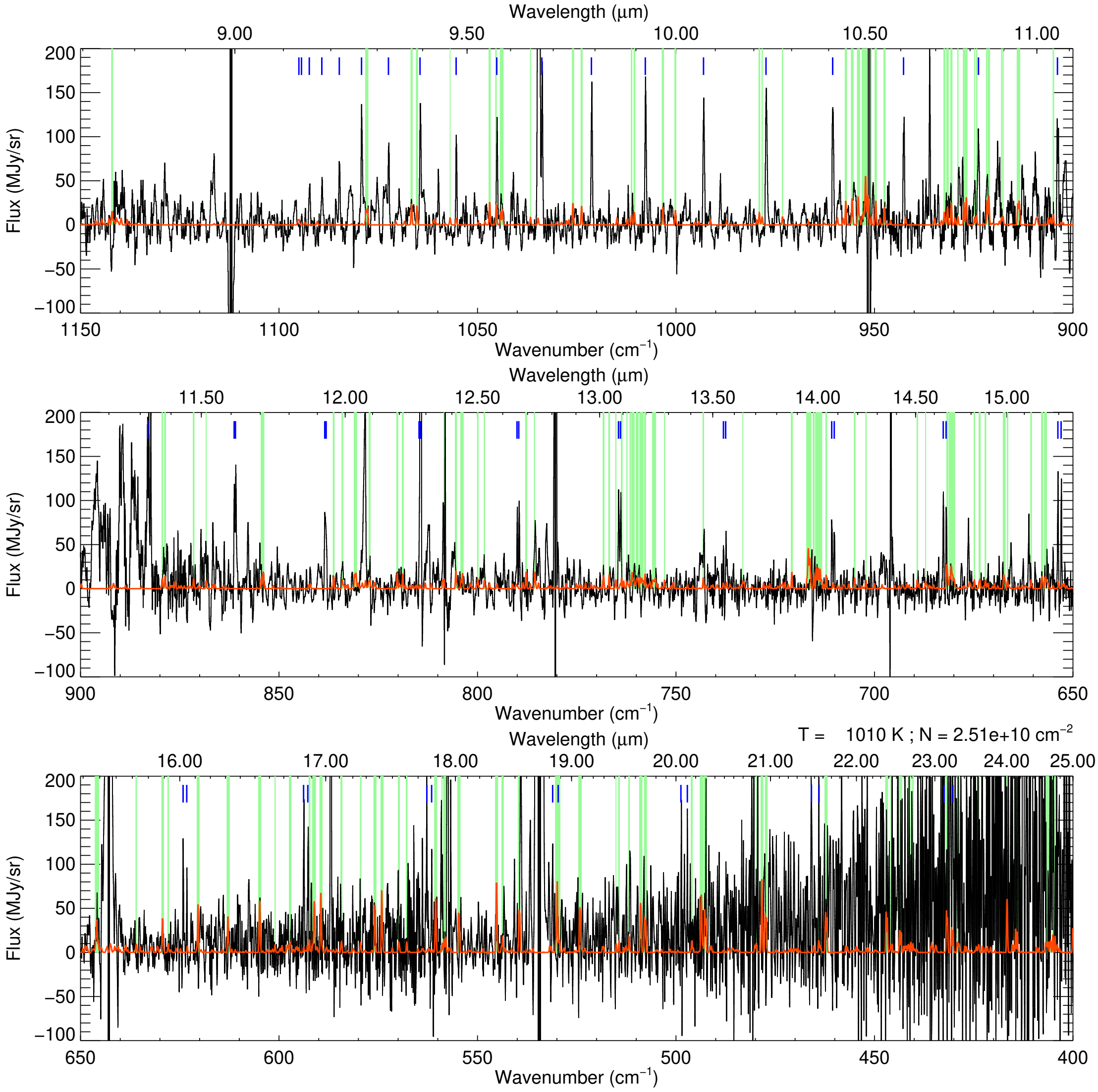

Fig. D.2. Comparison of the irradiated disk d203-506 continuum subtracted JWST spectrum to the CH_2^+ calculated LTE spectrum at 1010 K with a column density limit corresponding to 2.5×10^{10} cm^{-2} (red). The series of emission lines labeled with blue vertical marks corresponds to OH emission already reported in Zannese et al. (2024). The vertical green regions indicate the CH_2^+ lines used to constrain on the upper limit derived at that excitation temperature.